

## ARTICLE

# Seismic azimuthal amplitude variation with offset response analysis in coalbed methane reservoirs with aligned fractures using Biot theory

ZhaoJi Zhang<sup>1</sup> , Fei Gong<sup>1,2\*</sup>, GuanGui Zou<sup>1,2\*</sup>, Qiang Guo<sup>3</sup> , GuoWei Zhu<sup>1,2</sup>, and Hao Li<sup>1</sup>

<sup>1</sup>Department of Geophysics, College of Geoscience and Surveying Engineering, China University of Mining and Technology–Beijing, Beijing, China

<sup>2</sup>State Key Laboratory for Fine Exploration and Intelligent Development of Coal Resources, College of Geoscience and Surveying Engineering, China University of Mining and Technology–Beijing, Beijing, China

<sup>3</sup>Department of Geophysics, School of Resources and Geosciences, China University of Mining and Technology, Xuzhou, Jiangsu, China

### \*Corresponding authors:

Fei Gong  
(cupgongfei@163.com)  
GuanGui Zou  
(cumtzzg@foxmail.com)

**Citation:** Zhang ZJ, Gong F, Zou GG, Guo Q, Zhu GW, Li H. Seismic azimuthal amplitude variation with offset response analysis in coalbed methane reservoirs with aligned fractures using Biot theory. *J Seismic Explor.* 2026;35(2):025470118. doi: 10.36922/JSE025470118

**Received:** November 22, 2025

**Revised:** February 3, 2026

**Accepted:** February 10, 2026

**Published online:** March 4, 2026

**Copyright:** © 2026 Author(s). This is an Open-Access article distributed under the terms of the Creative Commons Attribution License, permitting distribution, and reproduction in any medium, provided the original work is properly cited.

**Publisher's Note:** AccScience Publishing remains neutral with regard to jurisdictional claims in published maps and institutional affiliations.

## Abstract

The development of coalbed methane (CBM) relies on high-precision reservoir prediction and lithological inversion. Seismic amplitude variation with offset (AVO) technology is an important tool for fine-scale reservoir characterization. However, the seismic AVO response of CBM reservoirs is complex and is affected by seismic rock physics parameters at different scales. Microscopically, aligned fractures in CBM reservoirs produce complex anisotropy due to formation inclination. At the macroscopic scale, the thickness of CBM reservoirs within seismic frequency bands is comparable to the seismic wavelength and should therefore be treated as a layered medium. In addition, pore fluid significantly affects seismic wave propagation. Consequently, determining the azimuthal AVO response of CBM reservoirs in relation to seismic rock physics parameters at different scales can support high-precision reservoir prediction and lithological inversion. In this study, the primary–primary wave reflection coefficient for a two-phase layered medium was derived using Biot's theory. Using this model, the response characteristics of the reflection coefficients with respect to seismic azimuth, aligned fracture parameters, reservoir thickness, and seismic main frequency were analyzed. A rotated staggered-grid finite-difference algorithm was employed to simulate wavefield characteristics separately for coal seams and surrounding strata. Seismic attributes were then used to characterize the seismic AVO response. The Z-direction seismic amplitude attributes and reflection coefficients showed similar trends in their responses to seismic rock-physical parameters. This study contributes to establishing a more precise seismic AVO response framework to support CBM reservoir prediction and high-quality lithological inversion.

**Keywords:** Azimuth; Amplitude variation with offset; Tilted transversely isotropic anisotropy; Fracture; Modeling

## 1. Introduction

Coalbed methane (CBM) is an unconventional natural gas with significant development potential.<sup>1,2</sup> The development of CBM depends on the availability of accurate reservoir predictions. Seismic amplitude variation with offset (AVO) response is a significant tool for reservoir prediction and characterization, as it contains information on underground lithology, pore space, fluid properties, and numerous other parameters.<sup>3</sup> Nevertheless, the seismic AVO response of CBM reservoirs is influenced by many factors, and the governing mechanisms remain unclear. At present, this limits its application as a reliable basis for lithological inversion and accurate CBM reservoir prediction.

Seismic AVO response characteristics are important indicators for reservoir prediction.<sup>4,5</sup> In studies of reservoir AVO responses, Xu *et al.*<sup>6</sup> used physical modeling to predict the AVO response laws of reservoirs of different sizes. Xiao *et al.*<sup>7</sup> investigated the AVO response characteristics of natural gas hydrates with varying properties and established a corresponding rock physics model. Gavin and Lumley<sup>8</sup> studied azimuthal AVO response characteristics in anisotropic media. Furthermore, Liu *et al.*<sup>9</sup> simulated the seismic response of horizontally fractured, thin, interbedded gas reservoirs using physical modeling techniques and analyzed the frequency-dependent AVO response under the combined effects of thin-layering and fractures. Xi and Yin<sup>10</sup> studied the seismic reflection laws of various sandstone formations and coal seams, summarizing the seismic response of common coal-bearing reservoir lithology combinations. Kumar *et al.*<sup>11</sup> developed a frequency-variant AVO (FAVO) model and combined it with logging data, demonstrating that reservoir stacking patterns are the primary factor controlling FAVO tuning response, followed by pore fluids. Following this, Ahmed *et al.*<sup>12</sup> developed a FAVO inversion method incorporating the quality factor, while Ouyang *et al.*<sup>13</sup> compared different FAVO inversion methods and demonstrated the superiority of P-wave dispersion for reservoir prediction, while Tian *et al.*<sup>14</sup> proposed a deep neural network-based method for predicting reservoir fluid parameters. The above studies show that research on seismic AVO responses mainly focuses on two aspects. On the one hand, it focuses on microparameters in unconventional reservoirs, analyzing the seismic AVO responses to factors such as reservoir microstructure, pore parameters, and pore fluids.<sup>5,7,11-19</sup> On the other hand, it investigates seismic AVO responses related to reservoir tectonic characteristics, such as reservoir thickness and seismic frequency.<sup>6,8,10,20-22</sup>

Exploration of CBM requires increasingly accurate seismic exploration to portray reservoir lithology, fracture

patterns, fluid types, and other microscopic parameters.<sup>23</sup> However, macroscopic factors such as reservoir thickness, azimuth, and seismic frequency can introduce uncertainties into reservoir prediction. Several issues remain unresolved in the above two areas of seismic AVO response research. In research focusing on microscopic factors, the seismic AVO response associated with fracture inclination remains unclear. Previous studies have shown that porosity fracture inclination angle significantly affects reservoir anisotropy and AVO response characteristics of reservoir rock.<sup>24,25</sup> Large-dip coal seams are widely distributed in China.<sup>26,27</sup> However, many current studies equate coal seams with high-angle fractures to horizontal transverse isotropic media. There are significant differences in AVO responses between these two, yet the seismic wavefield response in three-dimensional space with respect to fracture inclination angle has not been sufficiently considered.<sup>28-30</sup> In the study of the seismic azimuthal AVO response to macroscopic factors, the seismic AVO response of coal seams containing inclined fractures remains unclear. The thickness of unconventional natural gas reservoirs is often comparable to or smaller than the seismic wavelength, meaning that such reservoirs cannot be treated as a homogeneous infinite medium, but should instead be considered as a layered medium. Seismic wave reflections in a layered medium lead to interference effects that influence AVO response characteristics. Although the effects of reservoir thickness and seismic frequency are significant, the combined influence of these factors on the seismic AVO response of CBM reservoirs has not been adequately considered.

Rock physics can be used to quantitatively describe how rock microstructure, fracture morphology, and related parameters can affect elastic properties. Rock physics theory can be used to establish relationships among reservoir physical properties, microstructure, and seismic AVO response. Huang *et al.*<sup>31</sup> modeled the rock physics of CBM reservoirs and analyzed the relationship between intercept and gradient responses and CBM content. Wu *et al.*<sup>32</sup> quantified the effects of horizontal fractures on elasticity and various anisotropies in coal seams using rock physics modeling. Gong *et al.*<sup>33</sup> developed an anisotropic, multi-porosity rock physics model to predict the effects of different pore types on the elasticity and anisotropy of CBM reservoirs. These studies mainly focused on mapping the relationships between coalbed microstructure and elasticity and anisotropy, but several limitations remain. First, the seismic response of pore fluid under frequency-dependent conditions is often neglected, as the Gassmann equation is commonly applied to incorporate pore fluid without accounting for frequency effects in the modeling process.<sup>34</sup> Reflection and transmission of seismic waves

in the formation, based on the pore medium assumption, have not received much attention, which restricts accurate characterization of the seismic AVO response of coal seams. Second, fracture morphology is insufficiently accounted for in modeling, which typically treats fractures as vertical or horizontal distributions without considering their inclination angles. Furthermore, rock physics modeling primarily focuses on mapping the relationships between rock microstructures and elastic features, yet it does not explicitly depict the AVO response characteristics of seismic waves between strata. Seismic AVO response analysis combines rock physics modeling with coal stratigraphic features to determine the seismic AVO response characteristics under the influence of multiscale factors. This approach accurately portrays CBM reservoirs and enables high-precision lithological inversion.

Existing research has predominantly focused on the microphysical properties of reservoirs. Owing to the complexity of CBM reservoirs, studies that explicitly address the coupled effects of anisotropic fractures, seismic frequency dispersion, and thin-bed tuning on the azimuthal AVO response remain scarce. This gap hinders the accurate interpretation of seismic data for CBM reservoir characterization. In this study, the formulas for calculating the reflection coefficients of P-waves in a two-phase layered medium are first derived using Biot's theory. Combined with rock physics modeling, changes in the reflection coefficient in CBM reservoirs under multi-scale factors, such as fracture morphology, frequency, and layer thickness, are predicted. Seismic waveform response characteristics, including azimuth, oriented fracture porosity, fracture inclination, and fluid bulk modulus, were simulated using a finite-difference algorithm with a rotated staggered grid. The response laws of the seismic reflection coefficients and the seismic responses of CBM reservoirs with respect to multi-scale parameters, such as fracture morphology, frequency, and layer thickness, are summarized. This study provides a foundation for predicting CBM reservoirs and for high-precision lithological inversion by combining and guiding the seismic response law in complex media.

## 2. Methods

### 2.1. Coalbed methane reservoir modeling with aligned fracture inclination angle and azimuth

The pore structure of CBM reservoirs is highly complex. It consists of two types of pores: matrix pores and fractures.<sup>35</sup> Matrix pores and microscopic fractures have poor connectivity. These are the primary adsorption areas for CBM, whereas the macroscopic fractures have better connectivity and act as the main seepage channels

for coalbed water and CBM. Aligned fractures are the main source of anisotropy in CBM reservoirs.<sup>33,36</sup> Large-dip coal seams are widely distributed in China,<sup>26,27</sup> and fractures with different inclination angles can affect the azimuthal AVO response of CBM reservoirs. A rock-physics model of CBM reservoirs, incorporating multiple fracture inclination angles and azimuths, was developed to study the three-dimensional seismic AVO response of complex fracture systems. The Voigt–Reuss–Hill theory was used to construct the coal matrix, which consists of organic matter (OM) and ash. To restore the double-pore characteristics and anisotropy of the CBM reservoir, the self-consistent approximation theory was used to calculate the matrix pore, and the Schoenberg theory was used to calculate the aligned fractures. As shown in Figure 1, the bond transform rotates the medium around the x- and z-axes by a given angle. The fracture inclination angle is the angle between the fracture plane and the XOY plane, and the fracture azimuth is the angle with the Y-axis. The effect of pore fluid in coal cannot be ignored. Dispersion and attenuation in elastic media under the action of seismic waves mainly come from the pore fluid.<sup>37</sup> Within the seismic frequency band, the fluid relaxes within the pore space, and the pore pressure increment induced by seismic waves is equilibrated throughout the pore space.<sup>38</sup> Building on this, Biot<sup>39</sup> proposed a theoretical model of elastic wave dispersion attenuation on a macroscopic scale.<sup>39</sup> This model aims to restore the seismic response characteristics of CBM reservoirs under the influence of dispersion attenuation in seismic frequency bands. A rock-physics model of a CBM reservoir was constructed by incorporating a fluid phase into Biot's theory. Assuming the top and bottom plates of the coal bed are isotropic mudstone layers, the specific modeling process is shown in Figure 2.

### 2.2. Effect of aligned fractures on reflection coefficients of two-phase layered media

#### 2.2.1. Primary-primary wave reflection coefficient in two-phase layered media

The reflection coefficient bridges the gap between the formation's elastic properties and its seismic response. It can characterize the strength of reflected wave amplitudes and the AVO response of reservoirs. During seismic propagation in CBM reservoirs, the wavelengths of seismic wavelets are similar to the thickness of the coal seam. In this case, the coal seam can be considered a laminar medium. The P–P reflection coefficient (RPP) of a laminar medium differs somewhat from that of an infinite homogeneous medium in a half-space. Previous researchers have used the propagation matrix theory in layered media to study thin layers and to derive their equivalent reflection and transmission coefficients.<sup>40–43</sup> The RPP formulation for

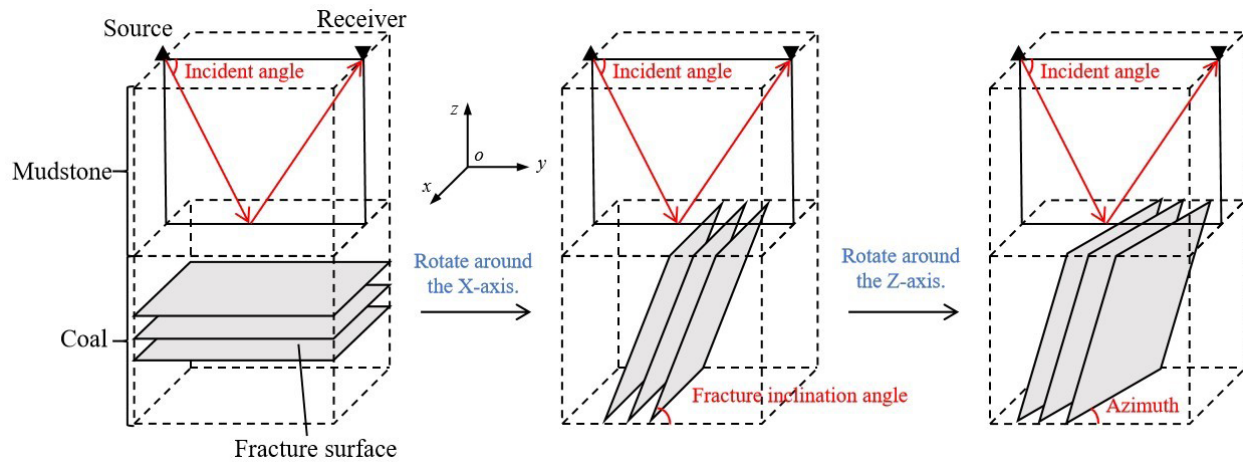


Figure 1. The coordinate transformations of the fracture inclination angle, incident angle, and azimuth

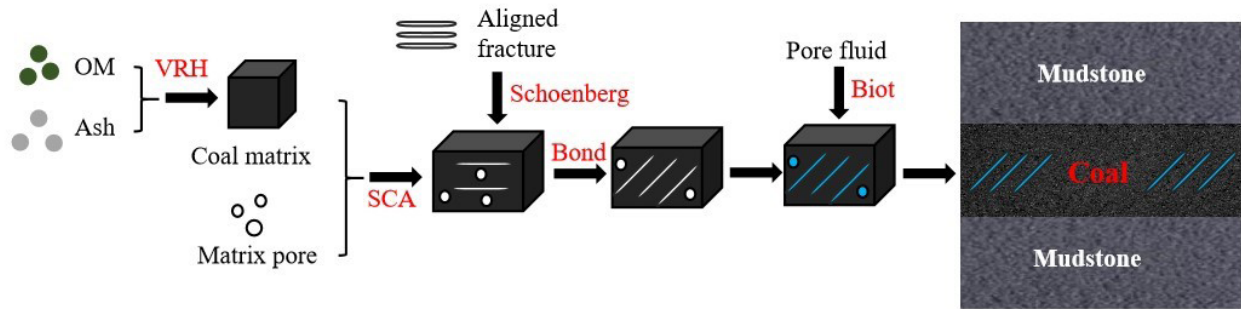


Figure 2. Rock physics model workflow

Abbreviations: OM: Organic matter; SCA: Self-consistent approximation; VRH: Voigt–Reuss–Hill.

two-phase layered media has been developed to enable more detailed characterization of CBM reservoirs within seismic frequency bands, supporting high-precision lithology prediction.

Forward modeling studies of thin layers typically employ the following two approaches:<sup>44</sup>

- Establishing reflection and transmission relationships for thin layers using time delay under arbitrary incidence angles.<sup>45,46</sup> This method is not suitable for investigating AVO characteristics of single thin layers.<sup>47</sup>
- Employing the propagation matrix theory for layered media to investigate thin-layer problems.<sup>40–43</sup> This approach further simplifies the P-wave and S-wave reflection theory for multi-layer media under arbitrary incidence angles to derive the P-wave reflection coefficient formula for a single thin layer.

We employed the theory of layered medium propagation to address thin-layer reflection phenomena. The generalized Hooke's law in two-phase media is shown

in Equation 1:

$$\begin{bmatrix} \sigma \\ s \end{bmatrix} = \begin{bmatrix} C & Q \\ Q & R \end{bmatrix} \begin{bmatrix} e \\ \varepsilon \end{bmatrix} \quad (1)$$

where  $C$  is the solid phase elastic stiffness matrix,  $\sigma$  is the force tensor in the solid phase, and  $s$  is the effective stress in the fluid phase.  $e$  and  $\varepsilon$  are the strains in the solid and fluid phase, respectively.  $Q$  is the fluid–solid coupling term, and the method for the value of  $Q$  in anisotropic media is derived from Dai *et al.*<sup>48</sup>  $R$  is the fluid pressure coefficient, which is determined by the bulk modulus of the fluid and the porosity of the medium,<sup>49</sup> as shown in Equation 2:

$$R = \frac{\phi^2}{(1 - \phi - \beta)C_r + \phi / K_f} \quad (2)$$

where  $\phi$  is the porosity,  $\beta$  is the ratio of the compression coefficients of the two-phase media particles and the skeleton;  $C_r$  is the compression coefficient of the two-phase media particles. and  $K_f$  is the fluid bulk modulus.

As shown in Figure 3, it is assumed that a P1 wave incident from an infinite homogeneous medium 1 passes through a series of thin layers (2 to  $m-1$ ) of medium and

finally enters the lower medium  $m$ , where it is reflected from the  $n$ -th layer. In the  $n$ -th layer, there are six waves: the incident P1 wave, the reflected P1 wave, the incident S wave, the reflected S wave, the incident P2 wave, and the reflected P2 wave. Their wave functions can be set as follows:

(i) Incident P1 wave (Equation 3):

$$\begin{cases} \varphi_{s1} = A_1 \exp[I(kx_1x + kz_1z - wt)] \\ \varphi_{f1} = A_{f1} \exp[I(kx_1x + kz_1z - wt)] \end{cases} \quad (3)$$

(ii) Incident P2 wave (Equation 4):

$$\begin{cases} \varphi_{s2} = A_2 \exp[I(kx_2x + kz_2z - wt)] \\ \varphi_{f2} = A_{f2} \exp[I(kx_2x + kz_2z - wt)] \end{cases} \quad (4)$$

(iii) Incident S wave (Equation 5):

$$\begin{cases} \psi_{s3} = A_3 \exp[I(kx_3x + kz_3z - wt)] \\ \psi_{f3} = A_{f3} \exp[I(kx_3x + kz_3z - wt)] \end{cases} \quad (5)$$

(iv) Reflected P1 wave (Equation 6):

$$\begin{cases} \varphi_{s4} = A_4 \exp[I(kx_4x + kz_4z - wt)] \\ \varphi_{f4} = A_{f4} \exp[I(kx_4x + kz_4z - wt)] \end{cases} \quad (6)$$

(v) Reflected P2 wave (Equation 7):

$$\begin{cases} \varphi_{s5} = A_5 \exp[I(kx_5x + kz_5z - wt)] \\ \varphi_{f5} = A_{f5} \exp[I(kx_5x + kz_5z - wt)] \end{cases} \quad (7)$$

(vi) Reflected S wave (Equation 8)

$$\begin{cases} \psi_{s6} = A_6 \exp[I(kx_6x + kz_6z - wt)] \\ \psi_{f6} = A_{f6} \exp[I(kx_6x + kz_6z - wt)] \end{cases} \quad (8)$$

where  $kx_i = \frac{\sin \theta_i}{v_i} w$ ,  $kz_i = \frac{\cos \theta_i}{v_i} w$ , in which  $\theta$  is the angle of incidence or reflection of the wave.  $\varphi_s$  and  $\varphi_f$  are the displacements in the solid and fluid phase, respectively.  $A_i$  and  $A_{fi}$  are the amplitudes of the solid and fluid parts, respectively, and let  $A_{fi} = b_i A_i$ ,  $v$  is the velocity of the wave,  $w$  is the circular frequency, and  $I$  is the imaginary unit.

From Snell's law, we can obtain Equation 9:

$$kx_i = \frac{\sin \theta_1}{v_1} w = \frac{\sin \theta_2}{v_2} w = \dots = \frac{\sin \theta_6}{v_6} w = \delta \quad (9)$$

The displacement component of the solid phase medium is set to be  $u = [u_x, u_y, u_z]^T$  and the displacement

component of the fluid phase medium be  $U = [U_x, U_y, U_z]^T$ . The displacement function can be expressed as Equation 10:

$$\begin{cases} u = \nabla \varphi_s + \nabla \times \psi_s \\ U = \nabla \varphi_f + \nabla \times \psi_f \end{cases} \quad (10)$$

where,  $\varphi_s$  and  $\psi_s$  are the bit functions of the P-wave and S-wave displacements in the solid phase, respectively.  $\varphi_f$  and  $\psi_f$  are bit functions of the P-wave and S-wave displacements in the fluid phase, and the Lorentz condition is satisfied between them. The displacements and displacement bits in the medium are shown in Equation 11:

$$\begin{cases} \varphi_s = \varphi_{s1} + \varphi_{s2} + \varphi_{s4} + \varphi_{s5} \\ \varphi_f = \varphi_{f1} + \varphi_{f2} + \varphi_{f4} + \varphi_{f5} \\ \psi_s = \psi_{s3} + \psi_{s5} \\ \psi_f = \psi_{f3} + \psi_{f5} \end{cases} \quad (11)$$

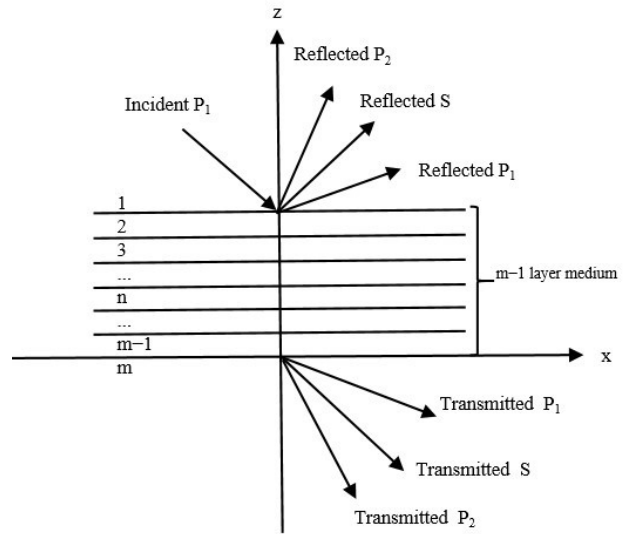


Figure 3. The propagation of seismic waves in layered media

Six boundary continuous conditions exist on the boundary plane of a two-phase medium:<sup>49,50</sup>

(i) Solid tangential displacement  $u_x$  continuum condition (Equation 12):

$$u_x^{(1)} = u_x^{(2)} \quad (12)$$

(ii) Solid normal displacement  $u_z$  continuum condition (Equation 13):

$$u_z^{(1)} = u_z^{(2)} \quad (13)$$

(iii) Continuous conditions of fluid mass  $M$  at the

interface (Equation 14):

$$M^{(1)} = M^{(2)} \quad (14)$$

where  $M = \rho_f \frac{\partial \varphi_f}{\partial z} + \rho_f \frac{\partial \psi_f}{\partial x}$ , and  $\rho_f$  is the fluid density.

(iv) Total normal stress  $\sigma_{zz} + s$  continuity condition (Equation 15):

$$\sigma_{zz}^{(1)} + s^{(1)} = \sigma_{zz}^{(2)} + s^{(2)} \quad (15)$$

(v) Solid tangential stress  $\tau$  continuum condition (Equation 16):

$$\tau^{(1)} = \tau^{(2)} \quad (16)$$

(vi) Fluid pressure  $P$  continuity conditions (Equation 17):

$$P^{(1)} = P^{(2)} \quad (17)$$

where  $s = -\phi P$ . The superscripts 1 and 2 represent physical quantities in different upper and lower media, respectively. A recursive formula is established to determine the boundary conditions at the top and bottom interfaces of the thin-layer medium. The detailed derivation process is provided in the Appendix.

$$\begin{bmatrix} u_x^{(n)} \\ u_z^{(n)} \\ M^{(n)} \\ \sigma_{zz}^{(n)} + s^{(n)} \\ \tau_{xz}^{(n)} \\ -P^{(n)} \end{bmatrix} = [H_{m-1}]_{z=Z(m-1)} \cdot d_{m-1} \cdots d_3 \cdot [H_2]_{z=Z(1)}^{-1} \cdot \begin{bmatrix} u_x^{(1)} \\ u_z^{(1)} \\ M^{(1)} \\ \sigma_{zz}^{(1)} + s^{(1)} \\ \tau_{xz}^{(1)} \\ -P^{(1)} \end{bmatrix} \quad (18)$$

where  $d_n = [H_n]_{z=Z(n-1)}^{-1} \cdot [H_{n-1}]_{z=Z(n-1)}$ .  $Z(n)$  is the coordinate of the  $n$ -th layer bottom on the  $z$ -axis. By substituting the wave function expressions for layer 1 and layer  $m$  into Equation 18 and combining with the method for deriving RPPs in infinite homogeneous half-space media published in past studies,<sup>51-53</sup> one can obtain the RPP for two-phase layered media.

### 2.2.2. Characterization of reflection coefficient response for multi-scale parameters

Based on the formula for RPP in a two-phase layered medium, this study discusses the response of RPP to seismic rock physics parameters at different scales. At the micro-scale of the coal seam, parameters affecting fracture morphology include fracture porosity and inclination.

Conversely, at the seismic macro-scale, factors such as seismic azimuth, coal seam thickness, and dominant wavelet frequency are important. This study aims to investigate the impact of multi-scale parameters on the RPP of a single coal seam. The top and bottom plates of the coal seam were set as mudstone with P-wave velocity of 3,500 m/s and S-wave velocity of 2,100 m/s. The coal matrix composition was set to 90% OM (with a bulk modulus of 5 GPa and a shear modulus of 2.5 GPa) and 10% ash (with a bulk modulus of 40 GPa and a shear modulus of 20 GPa). The matrix pore porosity was set to 3%, and the matrix pore aspect ratio was set to 0.2. The fracture aspect ratio was set to 0.01. To investigate the RPP response with respect to the azimuth, incidence angle, and slit inclination angle, the slit porosity was set to 2%, the seismic wavelet frequency was set to 50 Hz, and the coal seam thickness was set to 5 m. The responses of RPP to slit inclination angles and azimuths at different incidence angles are shown in Figure 4A-D, corresponding to incidence angles of 0–30°, respectively. As shown in Figure 4, the RPP value first increases and then decreases with increasing fracture inclination angle. The position of the peak depends on the incidence angle and azimuth. The RPP variation is axisymmetric about  $x = 180^\circ$ , and the larger the incidence angle, the more drastic the change on either side of the symmetry axis. As the fracture inclination angle and incidence angle increased, RPP gradually changed from a single peak to a double peak with azimuthal variation.

The incidence angle and azimuth were set to 0°. Figure 5 shows the response relationship between RPP and fracture porosity and fracture inclination angle, where Figure 5A-D correspond to incidence angles of 0–30°, respectively. As shown in Figure 5, the RPP initially increases and then decreases with increasing fracture inclination angle, peaking at approximately 35°. The fracture inclination angle is an important factor influencing the medium's anisotropy. The medium can be approximated as vertical transverse isotropy anisotropy at low fracture inclination angle, as horizontal transverse isotropy anisotropy at high fracture inclination angle, and at medium fracture inclination angle as tilted transverse isotropy anisotropy. The RPP values in different anisotropic media exhibited distinct patterns as fracture porosity increased. At a high fracture inclination angle, larger incident angles produced greater changes in RPP with respect to fracture porosity. At a low fracture inclination angle, the RPP response to fracture porosity depended on the incident angle: it increased with increasing fracture porosity at 0° and 10°, but decreased at 30°.

The Biot–Gassmann–Wood relationship describes the effect of mixed fluids on rock elastic properties



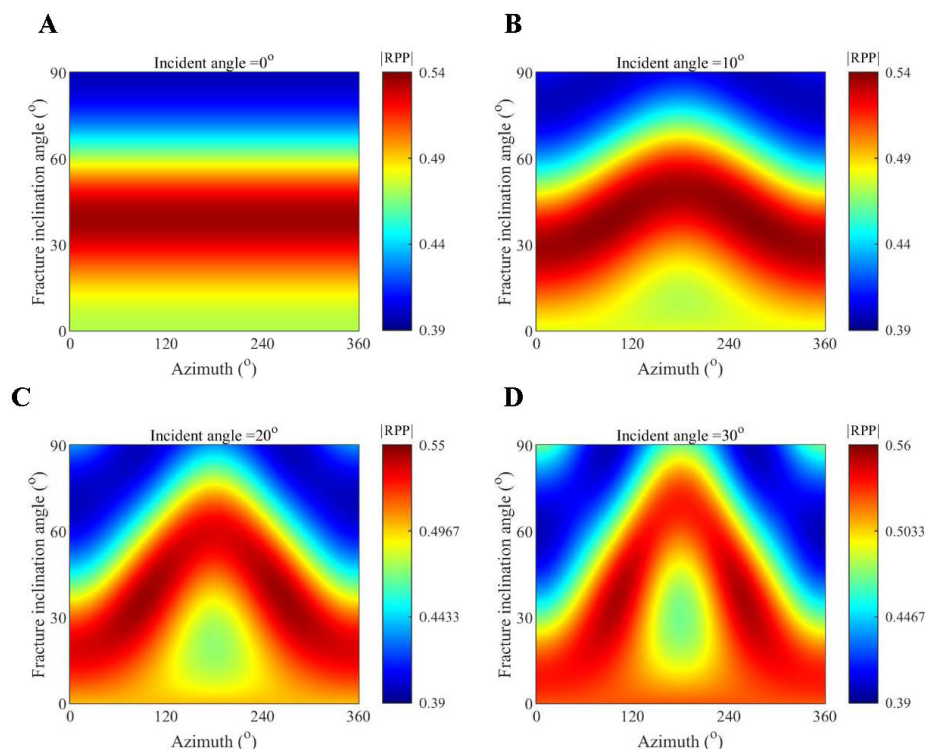


**Figure 4.** Response of the P–P reflection coefficient (RPP) with respect to fracture inclination angle and azimuth for different incident angles. (A) 0°, (B) 10°, (C) 20°, and (D) 30°.

across different frequencies.<sup>38,54</sup> The pore fluids in CBM reservoirs are complex and exist in adsorbed, free, and dissolved forms.<sup>33</sup> Different fluid storage forms and fluid properties mainly affect the bulk modulus and density of mixed pore fluids.<sup>55</sup> To study the response laws of the RPP with pore fluid parameters, the fracture inclination angle and azimuth of the CBM reservoir were set at 0°, and the porosity of the fracture was 2%. The response of the RPP of the CBM reservoir on the bulk modulus and density of the mixed fluid is shown in Figure 6. The RPP decreases as the bulk modulus of the pore fluid increases, while it varies little with density.

For layered media, layer thickness and seismic wavelet frequency are important parameters that affect the tuning effect. To investigate the effects of seismic wavelet frequency and coal seam thickness on the RPP, the fracture inclination angle was set to 45°, and the incidence angle and azimuth were set to 0°. The RPP was then predicted as a function of coal seam thickness and the dominant frequency of the seismic wavelet. As shown in Figure 7, when the seismic dominant frequency is low and the coal

seam is thin, the seismic wavelength is much larger than the coal seam thickness, resulting in a very small RPP. As the seismic wave frequency and coal seam thickness increased, the RPP of the coal seam showed a periodic relationship with both thickness and frequency. With increasing frequency, the RPP variation with coal seam thickness becomes increasingly pronounced.

### 3. Seismic wavefield simulation

#### 3.1. Numerical simulation method

The finite-difference method can simulate the wavefield characteristics of seismic waves in a medium. The resulting seismic record better reflects the reflection and refraction characteristics of seismic waves than the convolution method. High-precision finite differences can simulate the propagation laws of seismic waves in two-phase pore media and quantitatively analyze the seismic response characteristics of different fracture patterns in coal. The displacement and stress components can be expressed as Equation 19:

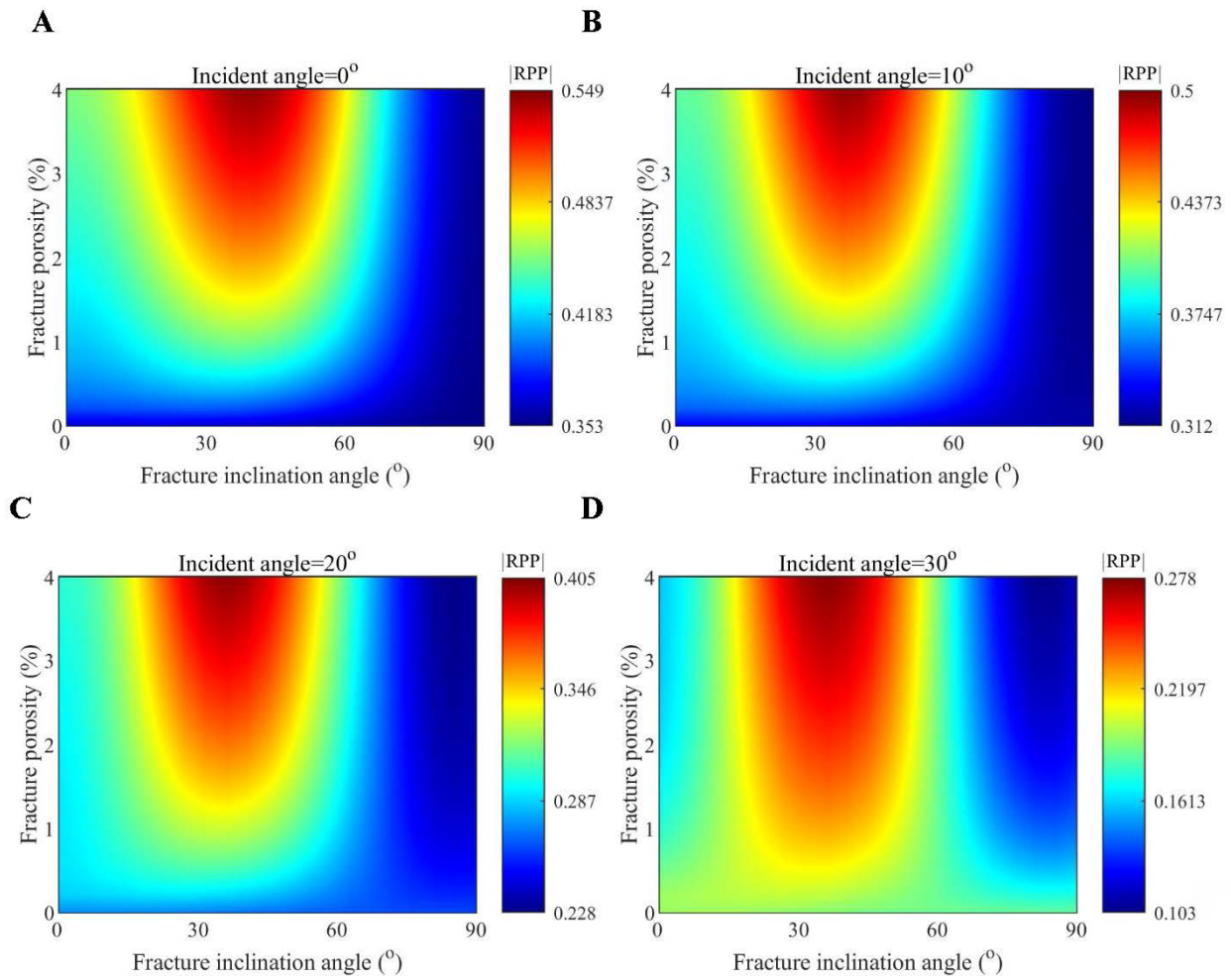


**Figure 5.** Response of the P-P reflection coefficient (RPP) with respect to fracture inclination angle and fracture porosity. (A) 0°, (B) 10°, (C) 20°, and (D) 30°.

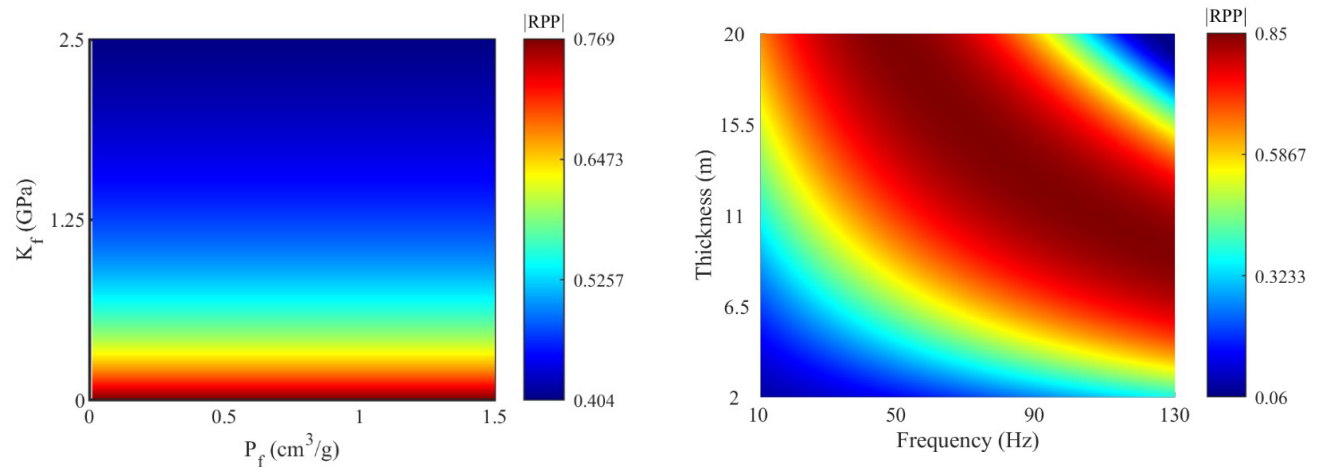


**Figure 6.** Response of the reflection coefficient with respect to pore fluid parameters. K<sub>f</sub>: bulk modulus of the pore fluid; P<sub>f</sub>: Pore fluid pressure; RPP: P-P reflection coefficient.

**Figure 7.** P-P reflection coefficient (RPP) on the response of coal seam thickness to seismic wave main frequency



$$\begin{cases}
\frac{\partial u_x}{\partial t} = (D_2 + D_3)b_{11}(u_x - U_x) - D_3 \left( \frac{\partial \tau_{xx}}{\partial x} + \frac{\partial \tau_{xz}}{\partial z} \right) + D_2 \frac{\partial s}{\partial x} \\
\frac{\partial u_y}{\partial t} = (D_2 + D_3)b_{22}(u_y - U_y) - D_3 \left( \frac{\partial \tau_{xy}}{\partial x} + \frac{\partial \tau_{yz}}{\partial z} \right) \\
\frac{\partial u_z}{\partial t} = (D_2 + D_3)b_{33}(u_z - U_z) - D_3 \left( \frac{\partial \tau_{xz}}{\partial x} + \frac{\partial \tau_{zz}}{\partial z} \right) + D_2 \frac{\partial s}{\partial z} \\
\frac{\partial U_x}{\partial t} = -(D_1 + D_2)b_{11}(u_x - U_x) + D_2 \left( \frac{\partial \tau_{xx}}{\partial x} + \frac{\partial \tau_{xz}}{\partial z} \right) - D_1 \frac{\partial s}{\partial x} \\
\frac{\partial U_y}{\partial t} = -(D_1 + D_2)b_{22}(u_y - U_y) + D_2 \left( \frac{\partial \tau_{xy}}{\partial x} + \frac{\partial \tau_{yz}}{\partial z} \right) \\
\frac{\partial U_z}{\partial t} = -(D_1 + D_2)b_{33}(u_z - U_z) + D_2 \left( \frac{\partial \tau_{xz}}{\partial x} + \frac{\partial \tau_{zz}}{\partial z} \right) - D_1 \frac{\partial s}{\partial z} \\
\frac{\partial \sigma_{xx}}{\partial t} = C_{11} \frac{\partial u_x}{\partial x} + C_{13} \frac{\partial u_z}{\partial z} + C_{14} \frac{\partial u_y}{\partial z} + C_{15} \left( \frac{\partial u_x}{\partial x} + \frac{\partial u_z}{\partial z} \right) + C_{16} \frac{\partial u_y}{\partial x} + Q_1 \left( \frac{\partial U_x}{\partial x} + \frac{\partial U_z}{\partial z} \right) \\
\frac{\partial \sigma_{zz}}{\partial t} = C_{13} \frac{\partial u_x}{\partial x} + C_{33} \frac{\partial u_z}{\partial z} + C_{34} \frac{\partial u_y}{\partial z} + C_{35} \left( \frac{\partial u_x}{\partial x} + \frac{\partial u_z}{\partial z} \right) + C_{36} \frac{\partial u_y}{\partial x} + Q_3 \left( \frac{\partial U_x}{\partial x} + \frac{\partial U_z}{\partial z} \right) \\
\frac{\partial \tau_{yz}}{\partial t} = C_{14} \frac{\partial u_x}{\partial x} + C_{34} \frac{\partial u_z}{\partial z} + C_{44} \frac{\partial u_y}{\partial z} + C_{45} \left( \frac{\partial u_x}{\partial x} + \frac{\partial u_z}{\partial z} \right) + C_{46} \frac{\partial u_y}{\partial x} \\
\frac{\partial \tau_{xz}}{\partial t} = C_{15} \frac{\partial u_x}{\partial x} + C_{35} \frac{\partial u_z}{\partial z} + C_{45} \frac{\partial u_y}{\partial z} + C_{55} \left( \frac{\partial u_x}{\partial x} + \frac{\partial u_z}{\partial z} \right) + C_{56} \frac{\partial u_y}{\partial x} \\
\frac{\partial \tau_{xy}}{\partial t} = C_{16} \frac{\partial u_x}{\partial x} + C_{36} \frac{\partial u_z}{\partial z} + C_{46} \frac{\partial u_y}{\partial z} + C_{56} \left( \frac{\partial u_x}{\partial x} + \frac{\partial u_z}{\partial z} \right) + C_{66} \frac{\partial u_y}{\partial x} \\
\frac{\partial s}{\partial t} = Q_1 \frac{\partial u_x}{\partial x} + Q_3 \frac{\partial u_z}{\partial z} + R \left( \frac{\partial U_x}{\partial x} + \frac{\partial U_z}{\partial z} \right)
\end{cases} \quad (19)$$

where

$$\begin{cases}
D_1 = \frac{\rho_{11}}{(\rho_{12}^2 - \rho_{11}\rho_{22})} \\
D_2 = \frac{\rho_{12}}{(\rho_{12}^2 - \rho_{11}\rho_{22})} \\
D_3 = \frac{\rho_{22}}{(\rho_{12}^2 - \rho_{11}\rho_{22})}
\end{cases} \quad (20)$$

and  $\rho_{11}$  and  $\rho_{22}$  denote the effective mass parameters in the solid and fluid phase, respectively.  $\rho_{12}$  is the mass parameter of the relative motion of the pore fluid.  $b_{ij}$  is the dissipation coefficient of the fluid moving relative to the skeleton.

The rotated staggered-grid finite-difference scheme was first invented, described, and applied by Saenger *et al.*<sup>56</sup> This technique is an extension of the traditional staggered-grid method. In models with density and velocity anomalies, the stability of the traditional finite-difference method is often insufficient.<sup>56</sup> The rotated staggered-grid method is used in anisotropic media to reduce errors caused by interpolation and to enhance the stability of numerical simulation.<sup>57</sup> Stability conditions for finite-difference calculations on rotated staggered grids were provided by Saenger *et al.*<sup>56</sup>, as shown in Equation 21:

$$\frac{\Delta t V_{\max}}{\Delta h} \leq 1 / \left( \sum_{k=1}^n |c_k| \right) \quad (21)$$

where  $\Delta t$  is the time step,  $V_{\max}$  is the maximum phase velocity,  $\Delta h$  is the spatial step, and  $c_k$  is the staggered grid spatial difference coefficient.

To simulate the half-space medium more accurately, the absorbing boundary condition is an important issue in the orthogonal process. The convolutional perfectly matched layer (CPML) technique was developed based on perfectly matched layers, which avoids the complexity of the conventional perfectly matched layer (PML).<sup>58,59</sup> CPML has adapted the form of the extended function  $s_x$  as follows:<sup>59</sup>

$$s_x = k_x + \frac{d_x}{a_x + iw} \quad (22)$$

where  $a_x \geq 0$ ,  $k_x \geq 0$ . When  $a_x = 0$ ,  $k_x = 1$ , it is the conventional PML standard form. The CPML absorbing boundary form is derived by convolving the spatial derivatives in the time domain.

### 3.2. Characterization of wavefields in coal

As a two-phase anisotropy medium, the propagation of seismic waves in coal seams is extremely complex. The fracture inclination angle was set to 45°, the azimuth to 0°, the model size to 200 m × 200 m, and the grid spacing to 1 m. A Ricker wavelet with horizontal polarization in the x direction of the solid phase was excited at the center of the model, with a main frequency of 50 Hz. The wavefield snapshot results were obtained at  $t = 35$  ms. Figure 8 shows the seismic wavefield result in the coal seam. As shown in Figure 8, the medium contains both fast and slow P- and S-waves. The slow P-wave has the smallest velocity. In the Biot theory, the slow P-wave originates from the relative motion of the solid phase and the fluid. It has a smaller velocity and stronger attenuation, and is essentially disregarded in seismic exploration. S-wave splitting originates from the difference between the S-wave polarization direction and the fracture plane. The polarization direction of fast S-waves is parallel to the fracture plane, whereas that of slow S-waves is perpendicular to it. Therefore, the difference between fast and slow S-waves originates from the rock's anisotropy. The difference between fast and slow P-waves originates from the interaction between the solid skeletal phase and the fluid phase of a two-phase pore medium.<sup>36</sup> The results

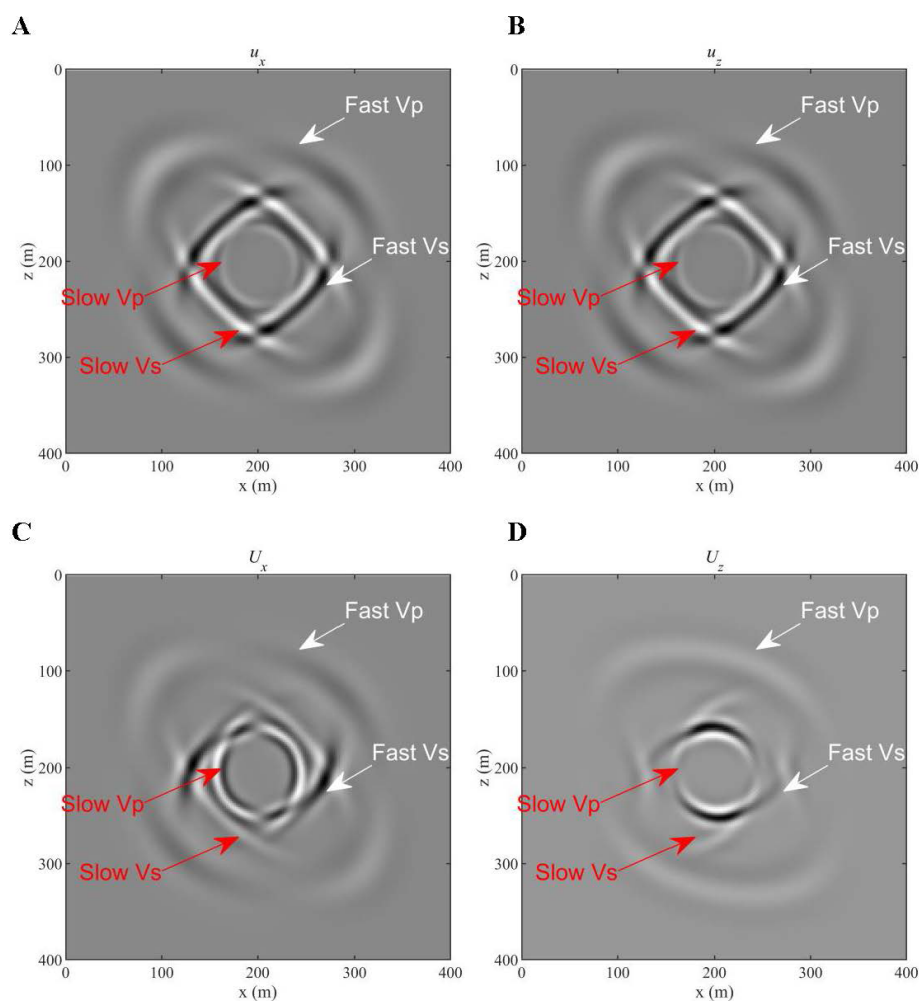


**Figure 8.** Wavefield snapshot of two-phase homogeneous TTI anisotropic media. (A) Solid phase x component, (B) solid phase z component, (C) fluid phase x component, (D) fluid phase z component.

Abbreviations: TTI: Tilted transversely isotropic; Vp: P-wave velocity; Vs: S-wave velocity.

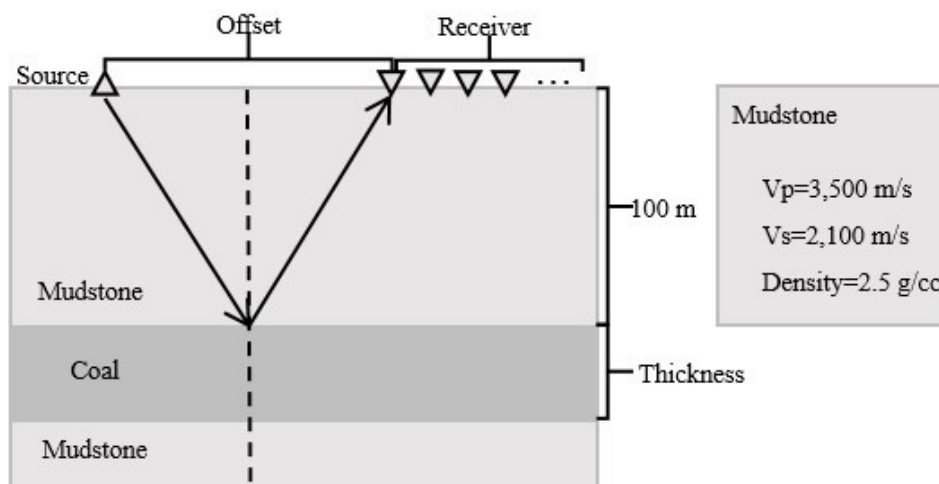


**Figure 9.** Coal-bearing strata model

Abbreviations: Vp: P-wave velocity; Vs: S-wave velocity.

demonstrate the effectiveness of the method in simulating seismic wave propagation characteristics in two-phase anisotropic media.

### 3.3. Characterization of seismic response of coalbed methane reservoirs

Seismic records in seismic exploration are mainly derived from reflected P-waves. To study the response of different seismic rock physics parameters in CBM reservoir seismic records, a seismic orthorectification model of CBM reservoirs was established, as shown in Figure 9. The coal seam top and bottom plates were set to be mudstone

(P-wave velocity 3,500 m/s, S-wave velocity 2,100 m/s). The composition of the coal matrix was set to 90% OM and 10% ash, the matrix pore porosity to 3%, matrix pore asp to 0.2, fracture asp to 0.01, fracture porosity to 1%, and the pore medium is saturated with water. The seismic wavelet frequency was 50 Hz, and the thickness of the coal seam was 5 m. Full-wavefield finite-difference simulations bridged the gap between theoretical reflectivity analysis and practical seismic interpretation. They validated whether the response trends predicted by the idealized plane-wave RPP formula hold in more realistic physical scenarios, including complex wave propagation, spherical

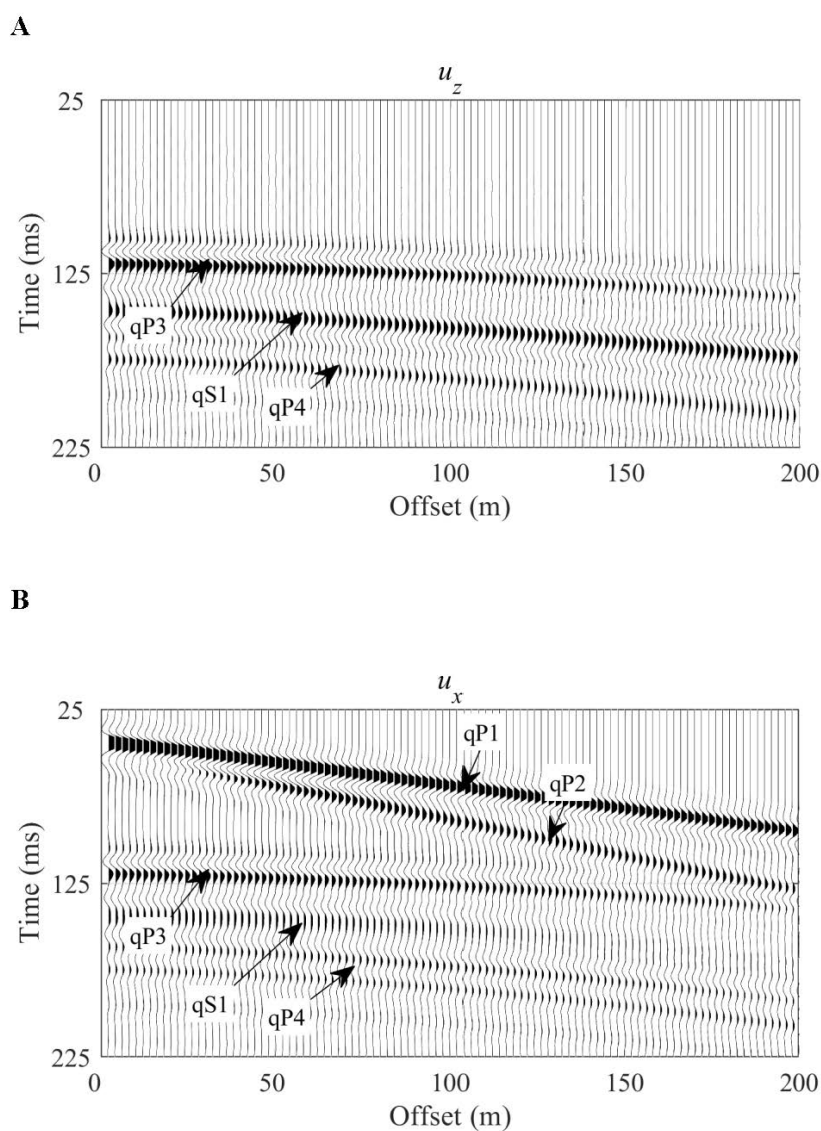


**Figure 10.** Seismic response of coalbed methane reservoirs. (A) Displacement in the z-direction. (B) x-direction displacement.

expansion, and full interference.

With the fracture inclination angle and azimuth set to  $0^\circ$ , Figure 10A and B shows the amplitudes  $u_z$  and  $u_x$  in the z and x directions, respectively, where qP1 and qP2 are the direct fast and slow P-waves, respectively. The qP3, qS1, and qP4 waves are the reflected fast P-, S-, and slow P-waves, respectively. There is a direct wave in the x direction, but no direct wave in the z direction because the line between the source and the wave detection point is parallel to the x-axis. The amplitude component of the direct wave in the z direction was zero. At near offsets, two P-waves overlapped. As the offset distance increased, the two P-waves gradually separated. qS1 wave velocity was larger than qP4, which matches the results in Figure 8. The direct waveform was identical to the Ricker wavelet used as the excitation source. Because the thickness of the coal seam is less than one-quarter of the wavelength, the reflected waveform becomes a superposition of two Ricker wavelets due to the seismic tuning effect. As shown in Figure 10, the finite-difference method employed in this study accurately described the reflection and transmission of seismic waves in a two-phase layered medium.

To study the influence of the fracture inclination angle on the response characteristics of seismic reflection waves, the fracture inclination angle was set to  $45^\circ$ , and the offset distance was set to 50 m. Figure 11A and B shows the variation of seismic amplitude with azimuth in z and x directions, respectively. It is difficult to observe the effects of microscopic rock-physics parameters on the seismic record. Therefore, seismic attributes were used to quantitatively describe the seismic response characteristics of different microscopic rock physics parameters. The constructed stratigraphic rock model had a single configuration and no lateral variation. The variation in seismic response

characteristics mainly comes from changes in amplitude. Therefore, seismic attributes derived from amplitude features were mainly used to quantitatively characterize the indicated seismic response features, and seismic records before and after 10 ms relative to the peak of the reflected wave were used to calculate the amplitude attributes. The changes of the selected seismic attributes with respect to the seismic azimuth are shown in Figure 11C, where the dashed line is the seismic attribute extracted from the amplitude in the x direction, and the solid line is the seismic attribute extracted from the amplitude in the z direction. As the azimuth increased from  $0^\circ$  to  $180^\circ$ , the seismic amplitude attributes in the z and x directions showed a sinusoidal pattern over half a cycle, with the amplitude of change in the z direction much larger than that in the x direction.

To study how the response characteristics of CBM reservoir-reflected waves are influenced by the fracture inclination angle, the azimuth was set to  $0^\circ$ , and the offset distance was 50 m. The seismic response characteristics for different azimuths were simulated using the finite-difference method. The amplitudes in the x and z directions are shown in Figure 12A and B. Figure 12C illustrates the relationship between seismic amplitude attributes and fracture inclination angle. As the fracture inclination angle increased from  $0^\circ$  to  $90^\circ$ , the seismic amplitude attributes in the z and x directions exhibited cosine and sine patterns, respectively, with the amplitude of change in the z direction larger. The fracture inclination angle was set to  $45^\circ$ , the offset distance to 50 m, and the azimuth to  $0^\circ$ . The responses of the amplitude and seismic amplitude attributes in the z direction and x direction with respect to the porosity of the fracture are shown in Figure 13A-C, respectively. With increasing fracture porosity, seismic

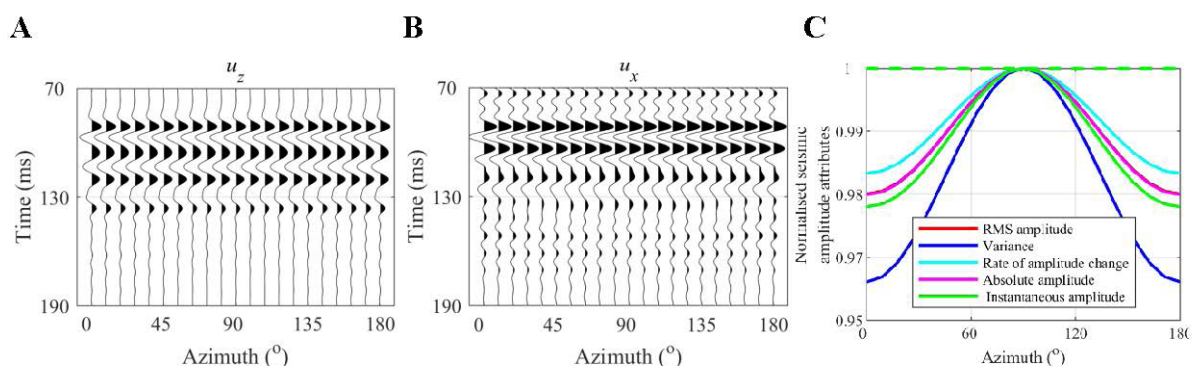


**Figure 11.** Response of seismic record and seismic amplitude attributes with respect to azimuth. (A) Displacement in the z-direction. (B) x-direction displacement. (C) Seismic amplitude attributes.



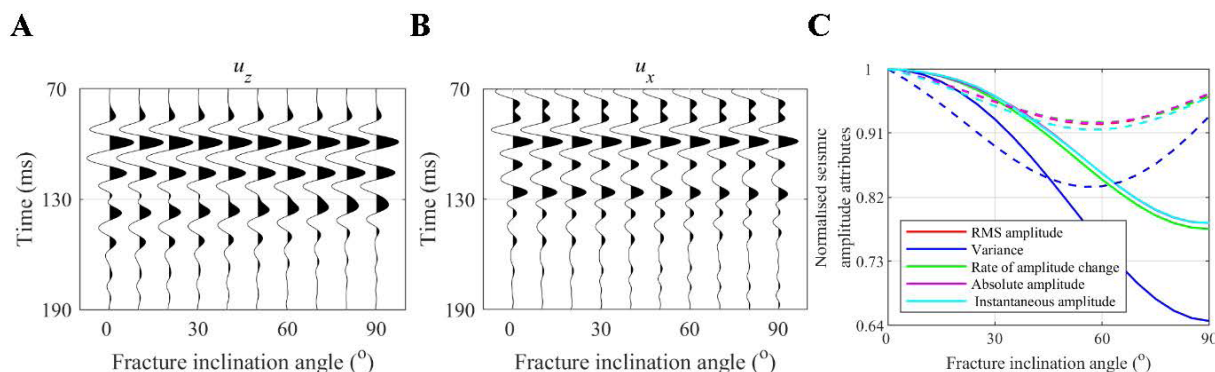


**Figure 12.** Response of seismic record and seismic amplitude attributes with respect to crack dip angle. (A) Displacement in the z-direction. (B) x-direction displacement. (C) Seismic amplitude attributes.

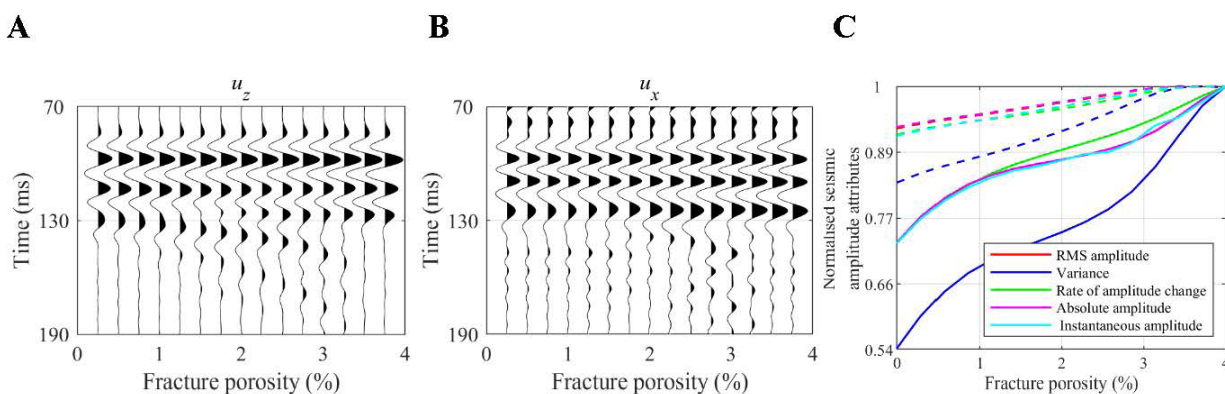


**Figure 13.** Response of seismic records and seismic amplitude attributes to crack porosity. (A) Displacement in the z-direction. (B) x-direction displacement. (C) Seismic amplitude attributes.

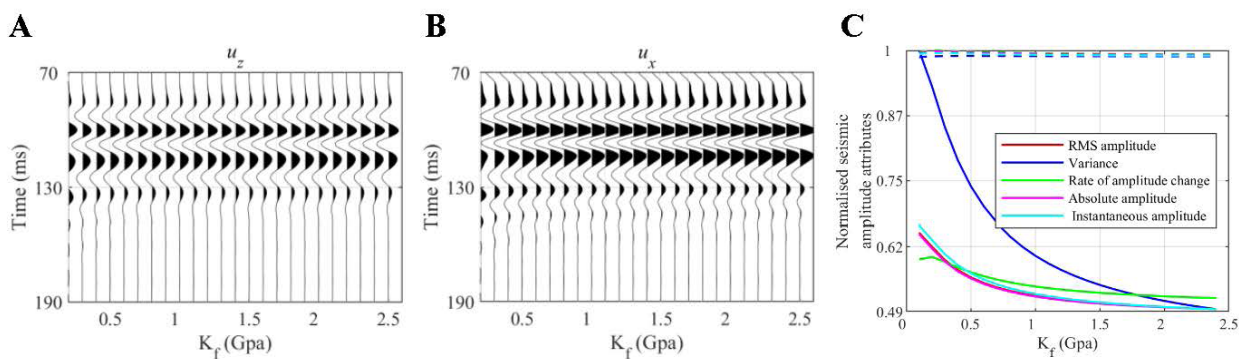


**Figure 14.** Response of seismic records and seismic amplitude attributes with respect to  $K_f$ . (A) Displacement in the z-direction. (B) x-direction displacement. (C) Seismic amplitude attributes.



amplitudes in both directions increased gradually but exhibited different patterns of change. The change in the z direction was larger than that x direction.

Figure 14 shows the effect of pore fluid equivalent bulk modulus on the seismic records of CBM reservoirs. As shown in Figure 14C, the seismic amplitude attributes in the x and z directions exhibit different trends as the bulk modulus of the mixed fluid increases gradually. The seismic amplitude attributes in the z direction gradually decreased, and the rate of decrease slowed; the change in the x direction is smaller than that in the z direction.

Combining Figures 11-14, it can be seen that with changes in azimuth, fracture parameters, and fluid parameters, the seismic records in the two-phase layered medium exhibited smaller changes, which were difficult to distinguish with the naked eye. The changes in seismic amplitude attributes were more obvious. x-direction seismic amplitude attributes were different from the z direction, and the changes of x-direction seismic amplitude attributes were smaller than those in the z direction. Comparing changes in seismic amplitude with the rock physics parameter in the z direction with those of RPP, it was found that the changes were the same. The RPP and seismic amplitude properties of a two-phase layered medium follow the same rules of change with rock physics parameters, which can reflect the medium's seismic AVO response characteristics to a certain extent. The correspondence between the derived RPP formula and seismic prediction results also demonstrates the formula's accuracy.

#### 4. Discussion

This paper derives the RPP for a two-phase layered medium using Biot's theory. A rock physics model of CBM reservoirs was constructed based on their pore-structure characteristics, accounting for aligned fracture inclination angles and azimuths. Using this model, we predicted the response of RPP to changes in azimuth, aligned fracture inclination angle, aligned fracture porosity, pore fluid parameters, coalbed thickness, and the main frequency of the seismic wavelet in two-phase layered media. We simulated the propagation characteristics of seismic waves in CBM reservoirs using the finite-difference method with a rotated staggered grid. The results demonstrate the phenomena of fast and slow P-wave splitting and S-wave splitting in the solid and fluid phases of the medium. This indicates that the finite-difference method can demonstrate the propagation laws of seismic waves in bidirectionally anisotropic media. To investigate the seismic response characteristics of CBM reservoirs, we constructed a single-layer stratigraphic model and predicted seismic responses

for different azimuths, fracture inclination angles, fracture porosity, and pore fluid bulk moduli. To highlight the rules governing changes in seismic features in relation to rock physics parameters, seismic amplitude attributes were used to quantify the seismic response. The seismic amplitude attributes in the z and x directions differed from the rock physics attributes, with the change in the z direction being larger than in the x direction. The seismic amplitude attributes in the z direction were similar to the RPP of the two-phase laminar medium. The RPP of the two-phase layered medium exhibited a high degree of similarity with the variation of seismic amplitude attributes. This study validated the seismic AVO response law in complex media and quantified the seismic response characteristics of CBM reservoirs under different seismic observation azimuths, fracture inclination angles, and other multi-scale rock physics parameters. It also supported accurate reservoir prediction and high-precision lithological inversion of CBM reservoirs.

#### 5. Conclusion

This study investigated the coupled effects of multi-scale parameters—fracture dip angle, fluid, frequency, and bed thickness—on the azimuthal AVO response in CBM deposits. The theoretical reflection coefficient model elucidates the independent mechanisms of each parameter, whilst full-waveform simulation validates their robustness in actual complex wavefields. It further explores application pathways for extracting these patterns from data via seismic attributes. This methodology provides a physically well-founded solution for precise seismic interpretation of complex reservoirs.

It should be noted that due to the unique characteristics of CBM reservoirs, coal seam AVO responses are influenced by multiple factors. These influencing factors stem from the complex physical process of seismic wave incidence and reflection within coal seams. This study simulated the impact of these factors on reflected wave amplitudes. Given the complexity of these influencing factors, reservoir prediction based on forward modeling principles requires integrating appropriate nonlinear reservoir prediction methods. This issue should be addressed in future work.

#### Acknowledgments

None.

#### Funding

This study was supported by the National Natural Science Fund Projects (42274165, 42474146), CNPC Innovation Fund (2024DQ02-0133), and the Fundamental Research Funds for the Central Universities (2024ZKPYDC03).

## Conflict of interest

Fei Gong and Qiang Guo are Editorial Board Members of this journal, but were not in any way involved in the editorial and peer-review process conducted for this paper, directly or indirectly. The authors declare they have no competing interests.

## Author contributions

*Conceptualization:* ZhaoJi Zhang, Fei Gong

*Formal analysis:* ZhaoJi Zhang

*Investigation:* ZhaoJi Zhang, Fei Gong

*Methodology:* ZhaoJi Zhang, Hao Li

*Visualization:* ZhaoJi Zhang, Hao Li

*Writing–original draft:* ZhaoJi Zhang

*Writing–review & editing:* GuanGui Zou, Qiang Guo, GuoWei Zhu

## Availability of data

The data that support the findings of this study are available from the corresponding author upon reasonable request.

## References

- Pan J, Ge T, Liu W, *et al.* Organic matter provenance and accumulation of transitional facies coal and mudstone in Yangquan, China: Insights from petrology and geochemistry. *J Nat Gas Sci Eng.* 2021;94:104076. doi: 10.1016/j.jngse.2021.104076
- Zhang D, He H, Ren Y, *et al.* A mini review on biotransformation of coal to methane by enhancement of chemical pretreatment. *Fuel.* 2022;308:121961. doi: 10.1016/j.fuel.2021.121961
- Guo Z, Li X. Azimuthal AVO signatures of fractured poroelastic sandstone layers. *Explor Geophys.* 2017;48(1):56-66. doi: 10.1071/eg15050
- Hu H, Xia K, Hiltebert F, Zhang Y. Amplitude-Versus-Angle Analysis of Local Angle-Domain Common Image Gathers With Prestack Gaussian-Beam Migration of Seismic Data. *IEEE Trans Geosci Remote Sens.* 2020;58(8):5969-5975. doi: 10.1109/TGRS.2020.2973654
- Wandler A, Evans B, Link C. AVO as a fluid indicator: A physical modeling study. *Geophysics.* 2007;72(1):C9-C17. doi: 10.1190/1.2392817
- Xu C, Chen C, Deng J, Di B, Wei J. A physical modelling study of the reservoir scale effect on amplitude variation with incidence angle. *J Geophys Eng.* 2019;16(6):1084-1093. doi: 10.1093/jge/gxz077
- Xiao K, Zou C, Shang J, Yang Y, Zhang H. Numerical simulation of AVO response characteristics from pore-filling gas hydrate in Qilian mountain permafrost, China. *Arab J Geosci.* 2019;12(12):379. doi: 10.1007/s12517-019-4548-0
- Gavin LJ, Lumley D. The effects of azimuthal anisotropy on 3D and 4D seismic amplitude variation with offset responses. *Geophysics.* 2019;84(6):C251-C267. doi: 10.1190/geo2018-0450.1
- Liu H, Ding P, Li X. Physical modeling of seismic responses in thin interbedded reservoirs with horizontal fracture. *Chin J Geophys.* 2021;64(8):2927-2940. doi: 10.6038/cjg202100167
- Xi Y, Yin X. Seismic Response Models and the AVO Simulation of Coal-Bearing Reservoirs. *Minerals.* 2022;12(7):836. doi: 10.3390/min12070836
- Kumar D, Zhao Z, Foster DJ, Dralus D, Sen MK. Frequency-dependent AVO analysis using the scattering response of a layered reservoir. *Geophysics.* 2020;85(2):N1-N16. doi: 10.1190/geo2019-0167.1
- Ahmed N, Weibull WW, Quintal B, Grana D, Bhakta T. Frequency-dependent AVO inversion applied to physically based models for seismic attenuation. *Geophys J Int.* 2022;233(1):234-252. doi: 10.1093/gji/ggac461
- Ouyang F, Liu XZ, Wang B, *et al.* The applicability and underlying factors of frequency-dependent amplitude-versus-offset (AVO) inversion. *Pet Sci.* 2023;20(4):2075-2091. doi: 10.1016/j.petsci.2023.02.011
- Tian Y, Stovas A, Gao J, Meng C, Yang C. Frequency-Dependent AVO Inversion and Application on Tight Sandstone Gas Reservoir Prediction Using Deep Neural Network. *IEEE Trans Geosci Remote Sens.* 2023;61:1-13. doi: 10.1109/tgrs.2023.3328183
- Chen SQ, Li XY, Wang SX. The analysis of frequency-dependent characteristics for fluid detection: a physical model experiment. *Appl Geophys.* 2012;9(2):195-206. doi: 10.1007/s11770-012-0330-8
- Si W, Di B, Wei J. Seismic response variation of tight gas sand for uniform and patchy saturation patterns. *J Appl Geophys.* 2015;116:167-172. doi: 10.1016/j.jappgeo.2015.03.010
- Wang X, Pan D. Application of AVO attribute inversion technology to gas hydrate identification in the Shenhu Area, South China Sea. *Mar Pet Geol.* 2017;80:23-31. doi: 10.1016/j.marpetgeo.2016.11.015

18. Yadav A, Mondal S, Yadav J, Chakraborty S. Direct hydrocarbon indicator analysis to predict reservoir in Deepwater Krishna-Godavari basin: a case study. *Explor Geophys*. 2023;54(6):625-635.  
doi: 10.1080/08123985.2023.2236119
19. Yang X, Cao S, Guo Q, Kang Y, Yu P, Hu W. Frequency-Dependent Amplitude Versus Offset Variations in Porous Rocks with Aligned Fractures. *Pure Appl Geophys*. 2016;174(3):1043-1059.  
doi: 10.1007/s00024-016-1423-8
20. Castoro A, White RE, Thomas RD. Thin-bed AVO: Compensating for the effects of NMO on reflectivity sequences. *Geophysics*. 2001;66(6):1714-1720.  
doi: 10.1190/1.1487113
21. Jin Z, Chapman M, Papageorgiou G, Wu X. Impact of frequency-dependent anisotropy on azimuthal P-wave reflections. *J Geophys Eng*. 2018;15(6):2530-2544.  
doi: 10.1088/1742-2140/aad882
22. Saeed W, Zhang H, Guo Q, *et al*. An integrated petrophysical-based wedge modeling and thin bed AVO analysis for improved reservoir characterization of Zhujiang Formation, Huizhou sub-basin, China: A case study. *Open Geosci*. 2020;12(1):256-274.  
doi: 10.1515/geo-2020-0011
23. Shi J, Wang S, Zhang H, *et al*. A novel method for formation evaluation of undersaturated coalbed methane reservoirs using dewatering data. *Fuel*. 2018;229:44-52.  
doi: 10.1016/j.fuel.2018.04.144
24. Wang P, Yao Z, Peng S, Hu S. A novel approximate formula on AVAZ of reflection and transmission qP in TTI media. *J Pet Sci Eng*. 2020;192:107280.  
doi: 10.1016/j.petrol.2020.107280
25. Xue J, Gu H, Cai C. Model-based amplitude versus offset and azimuth inversion for estimating fracture parameters and fluid content. *Geophysics*. 2017;82(2):M1-M17.  
doi: 10.1190/geo2016-0196.1
26. Shi B, Wang P. Research on Stability Control of Shields at Working Face with Large Dip Angle. *Energies*. 2023;16(15):5813.  
doi: 10.3390/en16155813
27. Tu H, Tu S, Yuan Y, Wang F, Bai Q. Present situation of fully mechanized mining technology for steeply inclined coal seams in China. *Arab J Geosci*. 2014;8(7):4485-4494.  
doi: 10.1007/s12517-014-1546-0
28. Elkibbi M, Yang M, Rial JA. Crack-induced anisotropy models in The Geysers geothermal field. *Geophys J Int*. 2005;162(3):1036-1048.  
doi: 10.1111/j.1365-246x.2005.02697.x
29. Kolesnikov Y, Fedin KV, Ngomayezwe L. Compression waves reflection from the low-velocity azimuthally anisotropic medium: a physical model study. *Geophys J Int*. 2020;221(2):1320-1326.  
doi: 10.1093/gji/ggaa031
30. Zhang J, Fan X, Huang Z, Liu Z, Fan Z, Liu L. In situ stress determination in isotropic and anisotropic rocks and its application to a naturally fractured reservoir. *Geomech Geophys Geo-Energy Geo-Resour*. 2023;9(1):80.  
doi: 10.1007/s40948-023-00584-6
31. Huang Y, Wei M, Malekian R, Zhen X. CBM Reservoir Rock Physics Model and Its Response Characteristic Study. *IEEE Access*. 2017;5:5837-5843.  
doi: 10.1109/access.2017.2687882
32. Wu H, Guo J, Ji G, Huang Y, Ding H, Lin P. Estimating the anisotropy of the vertical transverse isotropy coal seam by rock physics model-based inversion. *Geophys Prospect*. 2024;72(5):2064-2075.  
doi: 10.1111/1365-2478.13470
33. Gong F, Zou G, Zhang Z, Peng S, Wang G, Chen H. An anisotropic rock physics modeling for the coalbed methane reservoirs and its applications in anisotropy parameter prediction. *J Appl Geophys*. 2024;225:105381.  
doi: 10.1016/j.jappgeo.2024.105381
34. Mavko G, Mukerji T, Dvorkin J. *The Rock Physics Handbook*. 2nd ed. Cambridge University Press; 2010.  
doi: 10.1017/cbo9780511626753
35. Zhao M, Jin Y, Liu X, Zheng J, Liu S. Characterizing the Complexity Assembly of Pore Structure in a Coal Matrix: Principle, Methodology, and Modeling Application. *J Geophys Res Solid Earth*. 2020;125(12):e2020JB020110.  
doi: 10.1029/2020jb020110
36. Gong F, Huang A, Kang W, *et al*. The influence of lamination and fracture on the velocity anisotropy of tectonic coals. *Geophysics*. 2024;89(6):MR355-MR365.  
doi: 10.1190/geo2024-0033.1
37. Alkhimenkov Y, Quintal B. A simple and accurate model for attenuation and dispersion caused by squirt flow in isotropic porous rocks. *Geophysics*. 2023;89(1):MR1-MR10.  
doi: 10.1190/geo2023-0049.1
38. Mavko G, Nolen-Hoeksema RC. Estimating seismic velocities at ultrasonic frequencies in partially saturated rocks. *Geophysics*. 1994;59(2):252-258.  
doi: 10.1190/1.1443587
39. Biot MA. Theory of Propagation of Elastic Waves in a Fluid-Saturated Porous Solid. I. Low-Frequency Range. *J Acoust Soc Am*. 1956;28(2):168-178.  
doi: 10.1121/1.1908239

40. Carcione JM, Kosloff D, Behle A. Long-wave anisotropy in stratified media; a numerical test. *Geophysics*. 1991;56(2):245-254.  
doi: 10.1190/1.1443037
41. Chen T, Liu Y. Multi-component AVO response of thin beds based on reflectance spectrum theory. *Appl Geophys*. 2006;3(1):27-36.  
doi: 10.1007/s11770-006-0004-5
42. Kennett BLN, Kerry NJ. Seismic waves in a stratified half space. *Geophys J Int*. 1979;57(3):557-583.  
doi: 10.1111/j.1365-246x.1979.tb06779.x
43. Sidler R, Holliger K. Seismic reflectivity of the sediment-covered seafloor: effects of velocity gradients and fine-scale layering. *Geophys J Int*. 2010;181(1):521-531.  
doi: 10.1111/j.1365-246x.2010.04519.x
44. Wang Y, Yang C, Lu J. Dilemma faced by elastic wave inversion in thinly layered media. *Chin J Geophys*. 2018;61(3):1118-1135.  
doi: 10.6038/cjg2018L0404
45. Liu Y, Schmitt DR. Amplitude and AVO responses of a single thin bed. *Geophysics*. 2003;68(4):1161-1168.  
doi: 10.1190/1.1598108
46. Meissner R, Meixner E. Deformation of seismic wavelets by thin layers and layered boundaries. *Geophys Prospect*. 1969;17(1):1-27.  
doi: 10.1111/j.1365-2478.1969.tb02069.x
47. Pan W, Innanen KA. AVO/AVF analysis of thin beds in elastic media. In: *SEG Technical Program Expanded Abstracts 2013*. Society of Exploration Geophysicists; 2013.  
doi: 10.1190/segam2013-0587.1
48. Dai N, Vafidis A, Kanasevich ER. Wave propagation in heterogeneous, porous media; a velocity-stress, finite-difference method. *Geophysics*. 1995;60(2):327-340.  
doi: 10.1190/1.1443769
49. Geertsma J, Smit DC. Some aspects of elastic wave propagation in fluid-saturated porous solids. *Geophysics*. 1961;26(2):169-181.  
doi: 10.1190/1.1438855
50. Deresiewicz H, Skalak R. On uniqueness in dynamic poroelasticity. *Bull Seismol Soc Am*. 1963;53(4):783-788.  
doi: 10.1785/bssa0530040783
51. Rokhlin SI, Wang YJ. Equivalent boundary conditions for thin orthotropic layer between two solids: Reflection, refraction, and interface waves. *J Acoust Soc Am*. 1992;91(4):1875-1887.  
doi: 10.1121/1.403717
52. Tooley RD, Spencer TW, Sagoci HF. Reflection and transmission of plane compressional waves. *Geophysics*. 1965;30(4):552-570.  
doi: 10.1190/1.1439622
53. Ursin B, Stovas A. Reflection and transmission responses of a layered isotropic viscoelastic medium. *Geophysics*. 2002;67(1):307-323.  
doi: 10.1190/1.1451803
54. Mukerji T, Mavko G. Pore fluid effects on seismic velocity in anisotropic rocks. *Geophysics*. 1994;59(2):233-244.  
doi: 10.1190/1.1443585
55. Zou G, Zeng H, Peng S, Zhou X, Satibekova S. Bulk density and bulk modulus of adsorbed coalbed methane. *Geophysics*. 2019;84(2):K11-K21.  
doi: 10.1190/geo2018-0081.1
56. Saenger EH, Gold N, Shapiro SA. Modeling the propagation of elastic waves using a modified finite-difference grid. *Wave Motion*. 2000;31(1):77-92.  
doi: 10.1016/s0165-2125(99)00023-2
57. Jianxiong L, Chunjiao M. An efficient FDTD implementation of the CFS-PML based on the ADE method and its validation along with the PLRC method in dispersive media. In: Hong W, Yang G, eds. *2008 International Conference on Microwave and Millimeter Wave Technology*. IEEE; 2008:766-769.  
doi: 10.1109/icmmt.2008.4540510
58. Komatitsch D, Martin R. An unsplit convolutional perfectly matched layer improved at grazing incidence for the seismic wave equation. *Geophysics*. 2007;72(5):SM155-SM167.  
doi: 10.1190/1.2757586
59. Martin R, Komatitsch D. An unsplit convolutional perfectly matched layer technique improved at grazing incidence for the viscoelastic wave equation. *Geophys J Int*. 2009;179(1):333-344.  
doi: 10.1111/j.1365-246x.2009.04278.x

## Appendix

The boundary continuity conditions expressed in **Equations 12-17** may be represented in matrix form as follows:

$$\begin{bmatrix} u_x \\ u_z \\ M \\ \sigma_{zz} + s \\ \tau \\ P \end{bmatrix} = \begin{bmatrix} \frac{\partial \varphi_s}{\partial x} - \frac{\partial \psi_s}{\partial z} \\ \frac{\partial \varphi_s}{\partial z} + \frac{\partial \psi_s}{\partial x} \\ \rho_f \left( \frac{\partial \varphi_f}{\partial z} + \frac{\partial \psi_f}{\partial x} \right) \\ (C_{(3,:)} + C_{(7,:)}) \cdot \mathfrak{I} \\ C_{(5,:)} \cdot \mathfrak{I} \\ -\frac{1}{\phi} C_{(7,:)} \cdot \mathfrak{I} \end{bmatrix} \quad (\text{A1})$$

where  $C$  is the elastic stiffness matrix in a two-phase medium and  $\mathfrak{I}$  is a strain-dependent quantity. The wave function expression is taken from **Equation 11** into **Equation 18**:

$$\begin{bmatrix} u_x \\ u_z \\ m \end{bmatrix} = \begin{bmatrix} ikx_1 & ikx_2 & -ikz_3 & ikx_4 & ikx_5 & -ikz_6 \\ ikz_1 & ikz_2 & ikx_3 & ikz_4 & ikz_5 & ikx_6 \\ ib_1 \rho_f kz_1 & ib_2 \rho_f kz_2 & ib_3 \rho_f kx_3 & ib_4 \rho_f kz_4 & ib_5 \rho_f kz_5 & ib_6 \rho_f kx_6 \end{bmatrix} \cdot e$$

$$\begin{bmatrix} \sigma_{zz} + s \\ \tau \\ -P \end{bmatrix} = \begin{bmatrix} C_{(3,:)} + C_{(7,:)} \\ C_{(5,:)} \\ C_{(7,:)} / \phi \end{bmatrix} \cdot \mathfrak{I} \quad (\text{A2})$$

where

$$\mathfrak{I} = \begin{bmatrix} -kx_1^2 & -kx_2^2 & kx_3kz_3 & -kx_4^2 & -kx_5^2 & kx_6kz_6 \\ 0 & 0 & 0 & 0 & 0 & 0 \\ -kz_1^2 & -kz_2^2 & -kx_3kz_3 & -kz_4^2 & -kz_5^2 & -kx_6kz_6 \\ 0 & 0 & kx_3kz_3 - kz_3^2 & 0 & 0 & kx_6kz_6 - kz_6^2 \\ -2kx_1kz_1 & -2kx_2kz_2 & kz_3^2 - kx_3^2 & -2kx_4kz_4 & -2kx_5kz_5 & kz_6^2 - kx_6^2 \\ 0 & 0 & kx_3^2 - kx_3kz_3 & 0 & 0 & kx_6^2 - kx_6kz_6 \\ -b_1kx_1^2 - b_1kz_1^2 & -b_2kx_2^2 - b_2kz_2^2 & 0 & -b_4kx_4^2 - b_4kz_4^2 & -b_5kx_5^2 - b_5kz_5^2 & 0 \end{bmatrix} e \quad (\text{A3})$$

$$e = \begin{bmatrix} e^{ikz_1} & 0 & 0 & 0 & 0 & 0 \\ 0 & e^{ikz_2} & 0 & 0 & 0 & 0 \\ 0 & 0 & e^{ikz_3} & 0 & 0 & 0 \\ 0 & 0 & 0 & e^{ikz_4} & 0 & 0 \\ 0 & 0 & 0 & 0 & e^{ikz_5} & 0 \\ 0 & 0 & 0 & 0 & 0 & e^{ikz_6} \end{bmatrix} \cdot \begin{bmatrix} A_1 \\ A_2 \\ A_3 \\ A_4 \\ A_5 \\ A_6 \end{bmatrix} e^{i(\delta x - t\omega)} \quad (\text{A4})$$



The relationship between the continuity condition and the solid phase amplitude in the n-th layer can be simplified as:

$$\begin{bmatrix} u_x^{(n)} \\ u_z^{(n)} \\ M^{(n)} \\ \sigma_{zz}^{(n)} + s^{(n)} \\ \tau_{xz}^{(n)} \\ -P^{(n)} \end{bmatrix} = H_n \cdot \begin{bmatrix} A_1^{(n)} \\ A_2^{(n)} \\ A_3^{(n)} \\ A_4^{(n)} \\ A_5^{(n)} \\ A_6^{(n)} \end{bmatrix} \quad (A5)$$

where  $H_n$  is the relationship between the amplitude and the boundary continuity condition in the n-th layer of the medium, which is determined by Equations A1-A5. A recursive formula was developed to determine the quantitative relationship of the continuity condition at the top and bottom boundaries of the laminated medium:

$$\begin{bmatrix} u_x^{(n)} \\ u_z^{(n)} \\ M^{(n)} \\ \sigma_{zz}^{(n)} + s^{(n)} \\ \tau_{xz}^{(n)} \\ -P^{(n)} \end{bmatrix} = [H_{m-1}]_{z=Z(m-1)} \cdot d_{m-1} \cdots d_3 \cdot [H_2]_{z=Z(1)}^{-1} \cdot \begin{bmatrix} u_x^{(1)} \\ u_z^{(1)} \\ M^{(1)} \\ \sigma_{zz}^{(1)} + s^{(1)} \\ \tau_{xz}^{(1)} \\ -P^{(1)} \end{bmatrix} \quad (A6)$$